CuO doping tuned structural evolution, chemical durability and antibacterial activity of zinc phosphate glasses

GUO, Ruixin, ZHAO, Zhengkun, DENG, Wei, CHAKRABARTI, Anirban and XU, Kai <http://orcid.org/0000-0002-6847-1277>

CuO doping tuned structural evolution, chemical durability and antibacterial activity of zinc phosphate glasses

Ruixin Guo[a], Zhengkun Zhao[a,b], Wei Deng[c], Anirban Chakrabarti[a], Kai Xu[a,*]

[a] State Key Laboratory of Silicate Materials for Architectures, Wuhan University of Technology, Wuhan 430070, P. R. China

[b] Anhui Zhenghe Materials Technology Co., Ltd, Chuzhou 239000, P. R. China

[c] Materials and Engineering Research Institute, Sheffield Hallam University, Sheffield S1 1WB, UK

[*] Corresponding author

E-mail address: kaixu@whut.edu.cn (K. Xu).

Abstract:

This work investigated the impact of small amounts of CuO on the Cu species, structure, chemical durability, and antibacterial activity of zinc phosphate glasses. Glasses with a composition of $42P_2O_5$-30ZnO-20MgO-$8Na_2O$ (mol%) doped with 0–2.0 mol% CuO were prepared using the traditional melt-quenching method. Experimental findings indicate that doping 0.1 mol% CuO leads to the dispersion of metallic (Cu^0) particles exceeding 100 nm in size within the glass. These large Cu^0 particles can cause localized distortions in nearby phosphorus structural units, resulting in depolymerization of the glass network, which subsequently deteriorates the chemical durability of the glass matrix. The depolymerization process facilitates the release of zinc, which can enhance the antibacterial properties of glass against *E. coli*. Increasing the CuO content from 0.9–2.0 mol% resulted in the formation of mono- and divalent states of Cu (Cu^+ and Cu^{2+}), which appeared to enhance cross-linking between the phosphate units and gradually improved the chemical durability.

Keywords:

Zinc phosphate glass, antibacterial glass, Cu^0 particles, chemical durability

1. Introduction

Antibacterial glasses have garnered significant interest due to the adaptability of their glass network, which enables the incorporation of antibacterial metal ions and their controlled release [1]. When bacteria are exposed to these ions, bacterial growth is inhibited through mechanisms such as membrane disruption, respiration inhibition, protein inactivation, and DNA degradation [3]. Glasses doped with metallic ions such as silver, copper, and zinc have been extensively studied because of their broad-spectrum antibacterial activity, demonstrating potential applications in medical treatments and the remediation of contaminated soil and water [4-8].

Silver-doped antibacterial glasses are well-established and widely employed in consumer products and medical devices because silver ions exhibit superior antibacterial efficacy compared with copper and zinc ions. However, Ag^{+} is prone to reduce into Ag^{0} during glass melting and product usage, leading to the formation of Ag^{0} clusters, which impart a yellowish hue to silver-containing products [9,10]. In contrast, copper offers a lower cost while maintaining relatively similar antibacterial efficacy [11]. Despite this advantage, the strong steric constraints surrounding copper ions demonstrated by molecular dynamics simulations are attributed to their high ionic field strength, which limits ion exchange between H_3O^{+} and Cu^{+} ions, resulting in insufficient release of Cu^{+} and reduced antibacterial performance in Cu-containing glasses [12]. Consequently, extensive research has focused on elucidating the relationships among the composition, structure, and dissolution behavior of Cu-containing glasses to achieve better control over Cu release and enhance their

antibacterial effectiveness [7].

The valence states of copper incorporated into glass systems are variable, and the release of copper ions is influenced by the different copper forms, including Cu^{+}, Cu^{2+}, and Cu^{0} particles, which contribute to variations in antibacterial efficacy [4]. During the glass melting process, a redox equilibrium among $Cu^{2+} \leftrightarrow Cu^{+} \leftrightarrow Cu^{0}$ is established, which is strongly affected by the glass composition and melting conditions [12]. For example, more than 70% of Cu^{+} (Cu_2O) is formed at a high melting temperature of 1600 °C for 6 h without the addition of reducing agents. A high concentration of Cu^{+} ions facilitates H_3O^{+}/Cu^{+} ion exchange, thereby increasing Cu ion release and antibacterial efficacy. Copper ion release is also significantly influenced by the glass structure, which can be altered by the addition of copper oxide. In phosphate glasses, copper oxide disrupts P-O-P linkages and generates non-bridging oxygens, leading to the depolymerization of [PO_4] structural units [16]. However, in phosphate glasses containing high copper oxide contents (5–34 mol%), copper cations can act as cross-linking agents between non-bridging oxygens of two phosphate chains, increasing network polymerization and improving chemical resistance [17]. The content and oxidation state of copper in glass are thus critical factors affecting its release behavior and antibacterial properties. To the best of our knowledge, few studies have explored the impact of the addition of low copper content to zinc phosphate glasses on antibacterial efficacy and chemical durability.

This study examines the effects of low-CuO additions (≤2.0 mol%) on the chemical durability and antibacterial activity of P_2O_5-ZnO-MgO-Na_2O glasses,

synthesized using the traditional melt-quenching method. Trace additions of CuO (≤0.6 mol%) produced opaque red glass, which exhibited reduced durability against water, whereas higher additions (0.9–2.0 mol%) resulted in transparent green glasses with improved chemical durability. The type of Cu species, chemical durability, and antibacterial activity against *E. coli* in the glasses were analyzed as a function of the CuO content.

2. Experimental

2.1. Glass preparation

The nominal composition of the zinc phosphate glass matrix was $42P_2O_5$-30ZnO-20MgO-$8Na_2O$ (in mol%). Glasses containing up to 2.0 mol% CuO were prepared using the traditional melt-quenching method and are abbreviated based on their CuO content (e.g., Cu2.0 represents a sample with 2.0 mol% CuO). Analytical-grade reagents, including $NH_4H_2PO_4$, $Zn_3(PO_4)_2 \cdot xH_2O$, $MgCO_3$, Na_2CO_3, and CuO, were used for batch preparation.

For each glass, about 30 g of batch material was thoroughly mixed, placed in a corundum crucible, and preheated in a box furnace at 350 °C for 0.5 h to release moisture and gases such as NH_3 and CO_2. This preheating step minimized P_2O_5 loss during the glass melting process. The batch was then transferred to a furnace maintained at 1100–1200 °C, where it was melted for 1 h. The melt was poured onto a preheated brass plate and pressed with another brass plate to form thin glass plates. The quenched glass samples, with an initial thickness of about 2 mm, were subsequently polished into 1.5 mm thick sheets or ground into fine powders for further characterization.

2.2. Glass characterization

The density of the glass samples was determined using a Shimadzu densimeter (Shimadzu AUY120) based on Archimedes' principle, with silicone fluid (XIAMETER PMX-200, 1000 CS) serving as the immersion medium at ~25 °C. The average density was calculated from five repeated measurements of the glass plates.

The valence states of copper in the glass samples were analyzed using UV-visible (UV-vis) spectrophotometry (Shimadzu UV3600) and X-ray absorption spectroscopy (XAS). UV-vis spectra were obtained from optically polished glass samples over a wavelength range of 200–1200 nm, where the spectral line jumps at 710 and 820 nm attributed to detector switching, were smoothed using the Savitzky-Golay method. XAS measurements were conducted at the 1W1B station of the Beijing Synchrotron Radiation Facility (BSRF), with storage rings operating at 2.5 GeV and a maximum current of 250 mA. Measurements were performed in fluorescence mode using a Lytle detector, with samples pelletized into 8 mm diameter disks using graphite powder as a binder.

Extended X-ray absorption fine structure (EXAFS) spectra were processed according to standard procedures using the ATHENA module within the IFEFFIT software package. The spectra were obtained by subtracting the post-edge background from the overall absorption and normalizing against the edge jump step. The $\chi(k)$ data in k-space (1–12 $Å^{-1}$) were Fourier transformed to real (R) space using Hanning windows (dk = 1.0 $Å^{-1}$) to isolate contributions from various coordination shells. The quantitative data were derived through least-squares curve fitting in R space, employing

a Fourier transform k-space range of 1–12 $Å^{-1}$, using the ARTEMIS module of the IFEFFIT programs. The backscattering amplitude F(k) and phase shift Φ(k) were computed using the FEFF8.0 code.

The morphology of the precipitated particles in the samples was examined using a field emission scanning electron microscope (FE-SEM, JSM-7500F) operated at an accelerating voltage of 15 kV. The samples were prepared by embedding glass plates in epoxy resin, followed by grinding with 2000 SiC grit and polishing with an oil-based diamond suspension. The samples were then etched in diluted HF solution for 10 min and coated with platinum before analysis.

2.3. Antibacterial activity and elemental release tests

The antibacterial activity of the glasses was assessed against *E. coli* (ATCC, 25922) using the quantitative viable count method. *E. coli* was precultured in 3 mL of Luria-Bertani (LB) broth at 37 °C for 15 h under continuous shaking at 200 rpm. The concentration of the *E. coli* suspension was adjusted to 10^7 colony forming units (CFU)/mL. To assess antibacterial activity, 3 mL of the suspension was combined with 30 mg of glass sample (grain size: < 75 μm) and incubated at 37 °C for 2 h with shaking at 200 rpm. The resulting mixture was subsequently diluted 10^6 times, and 0.1 mL was inoculated onto LB agar plates, followed by incubation at 37 °C for 18 h. The number of viable bacteria was determined by counting the colonies that formed. The antibacterial activity was positively correlated with bacterial reduction (*R*), which was calculated as follows:

$$R = \left(1 - \frac{N_x}{N_{bc}}\right) \times 100\%$$

where N_x refers to the number of viable bacteria in glass sample Cux (x = 0, 0.1, 0.6, 1.2, 2.0), and N_{bc} indicates the number of viable bacteria in the blank control.

A leaching test was performed to investigate the dissolution and antibacterial properties of the glass samples. The samples were ground in an agate mortar and sifted through a 200-mesh sieve (75 μm). The powders were then cleaned ultrasonically with ethanol and dried overnight in an oven at 90 °C. Exactly 0.50 g of the powder (±0.5 mg) was placed in a 50 mL sealed Teflon vessel, which contained 50 mL of ultrapure water (pH ≈ 5.6). The vessel was kept at 37 ±1 °C in an oven for 2 h. The leachate was then filtered through a 0.45 μm filter, and the concentration of the released elements was analyzed using an inductively coupled plasma atomic emission spectrometer (ICP-AES, Leeman Labs, Prodigy 7). The tests were conducted in duplicate.

2.4. First-principle molecular dynamics simulations

The glass structures were examined using density functional theory (DFT)-based molecular dynamics (MD) simulations, which were performed with the Quickstep module [18] of the CP2K software package [19]. The hybrid Gaussian and plane-wave method (GPW) implemented in CP2K was utilized. The exchange-correlation energy was calculated by the Perdew-Burke-Ernzerhof (PBE) approximation [20], and dispersion interactions were treated using the DFT-D3 method [21]. A plane-wave cut-off of 500 Ry was selected for the electronic density, with a relative cut-off of 40 Ry. Valence electrons were described using double-zeta valence polarized basis sets and norm-conserving Goedecker-Teter-Hutter [22] pseudopotentials, all of which were optimized for solid-state applications (DZVP-MOLOPT-SR-GTH) for all the elements.

The initial structure was generated by randomly distributing atoms within the lattice. This structure was then heated to 3000 K for 20 ps and subsequently cooled in stages, following a temperature sequence of 3000 K, 2000 K, 1200 K, 800 K, and 300 K, with each stage lasting 10 ps. The final glass structures were simulated in a constant-pressure (N, P, T) ensemble with varying Cu^{2+} concentrations. A timestep of 1 fs was used throughout the MD simulations, and temperature control was maintained using the Nose-Hoover thermostat [23].

3. Results

3.1 Density, absorption and morphology analysis

The density (Fig. 1a) of the glass samples decreased from about 2.897 g/cm^3 to 2.849 g/cm^3 upon the addition of0.1 mol% CuO and then gradually increased to about 2.910 g/cm^3 as the CuO content rose to 2.0 mol%, slightly exceeding the density of the undoped sample (Cu0). Additionally, the molar volume displayed the opposite trend with the addition of CuO. However, assuming that Cu was incorporated into the glass network as Cu^{2+}, the calculated density (Fig. 1b) of the glass samples increased with the addition of CuO, indicating a distinct difference from the experimental density, especially for glasses containing 0.1−0.3 mol% CuO.

Fig. 2 shows the images and optical absorption spectra of glass samples doped with varying amounts of CuO. As displayed in the inset of Fig. 2, the undoped sample (Cu0) was transparent and colorless, whereas the glass turned opaque red with small amounts of CuO (0.1 to 0.6 mol%). Notably, when the CuO content reached 0.9 mol%, the color of the glass shifted to transparent green and became deeper in color as the CuO content

increased to 2.0 mol% as shown in the inset of Fig. 2b. The absorption spectrum of Cu0 showed a cut-off near 200 nm, whereas samples with smaller amounts of CuO (Cu0.1, Cu0.3, and Cu0.6) exhibited strong absorption below 600 nm, with red-shifting of the absorption edge as the CuO content increased. However, the absorbances of the glasses with 0.9, 1.2, and 2.0 mol% CuO decreased between 300 and 600 nm, and the absorption cut-off remained and displayed a redshift of about 100 nm, which can be attributed to the $3d^{10} \rightarrow 3d^{9}4s^{1}$ transitions of the Cu^{+} ions in the glasses [24]. These glasses also exhibited broad absorption bands between 600 and 1200 nm, centered at about 850 nm, which can be attributed to the d-d transitions of Cu^{2+} ions [25]. The absorbance of this band increased with increasing CuO content, indicating a higher concentration of Cu^{2+} ions. However, the absorption spectra of the glasses doped with 0.1, 0.3, and 0.6 mol% CuO did not exhibit any distinct surface plasmon resonance peak at 570 nm, which is characteristic of Cu^{0} metallic particles [26].

The presence of heterogeneously distributed spherical particles was detected from the FESEM study of the respective samples, as shown in Fig. 3. The inset of Fig. 3 shows the particle size distribution analysis of each sample. Notably, the size of these particles decreased as the CuO concentration increased to 0.6 mol%. For example, the average particle size in the Cu0.1 sample was larger than 100 nm, whereas it decreased to less than50 nm in the Cu0.6 sample.

3.2 Elemental release and antibacterial activity test

The release of P, Zn, Mg, and Na from different samples during 2 h of leaching at 37 ±1 °C is shown in Fig. 4a. The release patterns of these elements followed a similar

trend with increasing CuO content. Initially, the release of these elements sharply increased with the addition of 0.1 mol% CuO but quickly decreased as the CuO content increased to 0.6 mol%. After this, the amount released continued to decrease more slowly, as the CuO content reached 2.0 mol%. Furthermore, the elemental release from the Cu2.0 sample was similar to that of the undoped sample. As shown in Fig. 4b, the release of Cu increased almost linearly with increasing CuO content (Fig. 4b).

Fig. 5 displays the antibacterial activity of the different samples against *E. coli*, as indicated by the bacterial reduction rate (*R*). The *R* value increased with the addition of CuO to the glass samples, increasing from 4.5% to 27.2% as the CuO content increased from 0 to 2.0 mol%. Notably, the *R* value for the Cu0.1 glass was considerably greater than that for the Cu0.6 glass.

3.3 Radial distributions of Cu

The normalized Cu K-edge X-ray absorption near-edge structure (XANES) spectra of the Cu-doped Zn-phosphate glasses and the reference samples of the Cu foil, Cu_2O, and CuO are presented in Fig. 6a. Comparison of the valence states of Cu in the glass samples with these references can be inferred. The inset of Fig. 6a reveals that the absorption edge is minimally shifted for the opaque red glasses and progressively shifted to higher energies as the CuO content reached 2.0 mol%. This observation indicated that the average valence states of Cu remained relatively consistent in the red opaque glasses, whereas an increase in the Cu valence state was noted in the transparent green glass. The reference sample Cu_2O exhibited a lower energy peak at about 8982 eV, whereas the Cu foil and CuO samples presented broad low-energy tails at about

8981 eV and 8985 eV, respectively. A distinct pre-edge feature near 8984 eV was observed in the glass samples Cu0.3, Cu0.6, and Cu1.2, which was attributed to the 1s-4p electronic transition of Cu, recognized as the absorption edge of Cu^{+} [27]. Conversely, the spectra for samples Cu0.1 and Cu2.0 exhibited a shoulder-shaped feature near 8985 eV. A resemblance between the Cu foil and opaque glass samples was evident in the post-edge region spanning 8990–9012 eV. This feature included two peaks at about 8994 and 9003 eV for the Cu foil, which closely corresponded to peaks at about 8996 and 9002 eV for the opaque glass sample Cu0.6, which was consistent with the findings of Figueiredo et al. [31]. The broad post-edge feature was attributed primarily to Cu^{0} in the opaque glasses but became less prominent as the CuO content decreased.

Fig. 6b shows the Fourier transform of the Cu K-edge EXAFS spectra. Compared with those of the transparent glasses, the radial distribution patterns of the opaque red glasses were significantly different. For sample Cu0.1, the center of the radial distribution was located at about 1.9 Å, closely matching the reference Cu foil. As the CuO content increased to 0.6 mol%, this center position gradually shifted to about 1.6 Å, aligning with the reference values of Cu_2O and CuO. This shift indicated a change in the coordination environment where the primary nearest neighbor atom of Cu transitioned from Cu to O. On the other hand, the transparent green glasses presented a broad feature in terms of their radial distribution at about 1.4 Å, comparable to that of the reference samples Cu_2O and CuO, confirming that oxygen, as the dominant nearest neighbor atom, coordinates with Cu in the glass network.

4. Discussion

4.1 Analysis of Cu species and local structures

Complementary characterizations via optical absorption spectroscopy, FESEM and XANES analysis revealed that the Cu^0 particles were dispersed in the opaque red glasses (Cu0.1, Cu0.3 and Cu0.6) despite the absence of crystalline phases in the glasses recorded by X-ray diffraction (Fig. S1), whereas Cu^+ and Cu^{2+} were present in the transparent glasses (Cu0.9, Cu1.2 and Cu2.0). Linear combination fitting [27] was performed on the normalized XANES spectrum from 8970 to 9020 eV (Fig. S2) to analyze the valence states of the Cu species. The results in Fig. 7 indicate that the fraction of Cu^+ increased from about 0.34 to 0.42 as the CuO content increased from 0.1 to 0.6 mol% but decreased from about 0.44 to 0.08 as the CuO content further increased to 2.0 mol%. Simultaneously, the fraction of Cu^0 decreased from about 0.44 to 0.26, and the amount of Cu^{2+} increased from about 0.22 to 0.66 as CuO doping increased from 0.1 to 2.0 mol%. However, in opaque red glasses, the Cu^{2+} fraction remained nearly constant at about 0.22, irrespective of CuO addition. The absence of a distinct feature near 850 nm, indicative of Cu^{2+} in the optical absorption spectra (Fig. 2), suggested that minimal Cu^{2+} was present in the opaque glasses. Similarly, although low fractions of Cu^0 were noted in the transparent green glasses (Fig. 7), the absence of the SPR feature of the Cu^0 particles was observed, as shown in Fig. 2. Thus, Cu predominantly exists as Cu^0 and Cu^+ in opaque red glasses and as Cu^+ and Cu^{2+} in transparent green glasses [16].

In this study, Cu was introduced into the batch as CuO, and the reduction of copper

from Cu^{2+} to Cu^{0} and Cu^{+} at lower CuO additions (0.1–0.6 mol%) was likely due to the high melting temperature and the nominally reducing conditions influenced by the glass composition [12]. However, with increasing CuO content, Cu acted as a glass modifier, disrupting P-O-P bonds and generating more non-bridging oxygens. Higher CuO concentrations (0.9–2.0 mol%) also increased the glass basicity, leading to a greater negative charge on the constituent oxygen atoms in the glass. This can stabilize the higher oxidation states of copper ions (Cu^{+} and Cu^{2+}) to maintain electroneutrality within the transparent glasses [16].

The EXAFS spectral profiles in R space, as depicted in Fig. 6b, provided insights into the evolution of the Cu local structure across varying CuO additions. The fitted spectra and structural parameters derived from the simulation of EXAFS data in *k*-space are presented in Fig. S3 and Table S1. The average Cu-O atomic distance for samples Cu1.2 and Cu2.0 was about 1.92 Å, which lies between the bond distances of Cu^{+} in Cu_2O (~1.84 Å) and those of Cu^{2+} in CuO (~1.95 Å) [33]. Compared with the sharper peaks of Cu_2O (~1.5 Å) and CuO (~1.6 Å) (Fig. 6b), a broad peak centered at about 1.4 Å in samples Cu1.2 and Cu2.0 suggested significant distortion of the local Cu structure in the glass compared with its crystalline counterparts. This indicated that the Cu^{+} and Cu^{2+} ions were coordinated with the oxygen atoms in the glass matrix and acted as intermediate cations within the network. These intermediate Cu cations could enhance the cross-linking within the phosphate chains, as the fractions of Cu^{+} and Cu^{2+} ions increased with increasing CuO content. Such structural modifications could influence key glass properties, including chemical durability, by altering network connectivity

and stability [17].

4.2 Modification of glass properties by different Cu species

The variation in the Cu species dispersed within the glasses significantly influenced their structure and properties. The densities of the opaque red glasses, which contained Cu^0 particles and Cu^+ ions, were lower than those of the transparent glasses containing Cu^+ and Cu^{2+} ions, while the molar volumes followed an inverse trend (Fig. 1a). The normalized element release profiles of the major elements P and Zn from the glasses (shown in Fig. 8) show congruent release behavior, which is consistent with previous studies [2] and is indicative of uniform glass dissolution. The P and Zn release concentrations from the transparent glasses were markedly lower than those from the opaque glasses, highlighting that the dispersion of the Cu^0 particles severely compromised the chemical durability of the glasses. The transparent glasses of Cu0.1 (colorless) and Cu0.6 (light blue) maintained stoichiometry equivalent to that of opaque Cu0.1/Cu0.6 glasses, which were prepared while remaining free of Cu^0 particles. The P release concentrations from these transparent samples, represented as hollow dots in Fig. 4a, were significantly lower than those from their opaque counterparts, which was attributed directly to the deterioration in chemical durability due to the presence of dispersed Cu^0 particles.

The release of Cu and Zn, which are antibacterial agents, plays a critical role in the antibacterial activity of Cu-doped zinc phosphate glasses against *E. coli*. The undoped sample Cu0 showed low bacterial reduction (4.54%) despite the release of ~165 ppm Zn at 37 °C over 2 h, indicating that similar concentrations of Zn released

from glasses (Cu0.6, Cu1.2, and Cu2.0) alone did not predominantly enhance antibacterial activity (Fig. 4a and 5). The antibacterial efficacy improved with increasing CuO content (0.6–2.0 mol%), corresponding to an increase in Cu release from ~2.9 ppm to ~7.5 ppm under the same conditions. However, sample Cu0.1 demonstrated greater bacterial reduction than sample Cu0.6 despite lower Cu release (~0.5 ppm) but significantly greater Zn release (~270 ppm compared with ~196 ppm for Cu0.6), which can be attributed to the compromised chemical durability caused by the Cu^0 particles contributing to the observed effects.

4.3 Mechanism of Cu species on modifying chemical durability

The chemical durability of glass can be influenced by the degree of polymerization of its network. However, the Raman spectral profiles (Fig. S4) of glasses with varying CuO contents showed minimal changes. To further investigate the effects of the Cu^0 particles on the local structure, density functional theory (DFT)-based molecular dynamics (MD) simulations were performed. The structures of model glasses with a base composition of $42P_2O_5$-30ZnO-20MgO-$8Na_2O$ (in mol%) doped with 0, 1, and 13 mol% CuO are illustrated in Fig. 9. In the case of model glass Cu13 (Fig. 9c), the Cu atoms were closely packed into a cluster to simulate the dispersion of the Cu^0 particles in opaque glasses. The densities of model glasses Cu0, Cu1, and Cu13 were 2.91 g/cm^3, 2.87 g/cm^3, and 2.72 g/cm^3, respectively. The dispersion of the Cu^0 particles clearly led to a decrease in the density of the model glass, which is consistent with the experimental findings shown in Fig. 1a. The radial distribution functions of glasses doped with different Cu species, namely, Cu ions (Cu1) and Cu clusters (Cu13), are presented in

Fig. 9d. The radial distribution patterns of the P-O and O-O pairs exhibited negligible changes between the model glasses Cu0 and Cu1 containing ionic Cu. However, when Cu was dispersed as Cu^0 clusters in model glass Cu13, the radial distribution of P-O and O-O pairs shifted noticeably to longer distances, particularly for the O-O pair. This suggested that the local structure of the glass was significantly altered by the dispersion of the Cu^0 particles.

The reduced Cu^0 species can aggregate to form Cu^0 particles ranging from ~20 nm to ~250 nm, which are dispersed throughout the glass matrix (Fig. 3), giving glasses (Cu0.1, Cu0.3, and Cu0.6) an opaque red color [33]. Relatively large particles can cause persistent distortions in nearby phosphorus structural units [35]. This may contribute to the depolymerization or weakening of the P-O-P bonds in the glass network (Fig. 10a), leading to a decrease in chemical durability [36]. Furthermore, as CuO was added (0.1–0.6 mol%) to opaque glasses, the reduction in the Cu^0 particle size and the buildup of ionic Cu^+ enhanced the cross-linking of non-bridging oxygen atoms from adjacent phosphate units in the glass network, resulting in improved chemical durability [37]. Likewise, an increase in the ionic state of Cu with increasing CuO content (0.9–2.0 mol%) in transparent glasses promoted the cross-linking of the glass network, which may enhance chemical durability [17]. However, a low amount of smaller Cu^0 particles or clusters might disperse in the glass host under the detection limits of the UV-vis, SEM, and XANES techniques, leading to depolymerization or weakening of the P-O-P bonds in the glass network. Hence, the chemical durability of the transparent glass with 0.9–2.0 mol% CuO was deteriorated than that of the undoped glass sample.

The nanosized Cu^0 particles were expected to disperse within the glass matrix and interact with the glass network through physical bonds rather than chemical bonds (Fig. 10b). The interfacial voids between the Cu^0 particles and the glass network might form, and their volume can increase with particle coarsening, resulting in relatively high molar volumes, as observed in opaque red glasses (Fig. 1a). This can increase the reaction area for glass dissolution, which might accelerate elemental release from opaque glasses.

5. Conclusions

Zinc phosphate glasses doped with 0–2.0 mol% CuO were prepared using the traditional melt-quenching method. With the addition of 0.1–0.6 mol% CuO, the predominant valence states of the Cu in the glass samples were Cu^0 and Cu^+. Cu^0 was observed to aggregate, forming Cu^0 particles that imparted an opaque red coloration to the glasses. The formation of large Cu^0 particles could induce structural distortions in nearby phosphorus units, leading to depolymerization of the glass network and a consequent deterioration in the chemical durability of the glass matrix. Increasing the CuO content to 0.9–2.0 mol% resulted primarily in the presence of Cu in ionic states, such as Cu^+ and Cu^{2+}, imparting a transparent green color to the glass. The ionic Cu^+ and Cu^{2+} appeared to enhance cross-linking between phosphate units, thereby gradually improving chemical durability, although the presence of non-bridging oxygen associated with CuO addition could negatively impact the polymerization of the glass network. Furthermore, the antibacterial activity of the glasses against *E. coli* increased with increasing CuO content in general. And the antibacterial activity of glass against

gram-positive bacteria such as S. aureus needs further assessment to extend potential practical applications. The long-term dissolution behavior of glass containing different Cu species will be investigated in future studies.

CRediT authorship contribution statement

Ruixin Guo: Methodology, Data curation, Investigation, Writing – original draft. **Zhengkun Zhao**: Data curation, Funding acquisition. **Wei Deng**: Writing – review & editing. **Anirban Chakrabarti**: Writing – review & editing. **Kai Xu**: Methodology, Data curation, Writing – review & editing, Supervision, Funding acquisition.

Acknowledgements

The authors gratefully acknowledge the project of Science and Technology Plan (Grant No. 2022CX006) from Chuzhou government.

References

[1] F.N.S. Raja, T. Worthington, L.P.L. Souza, S. B. Hanaei, and R. A. Martin, Synergistic antimicrobial metal oxide-doped phosphate glasses; a potential strategy to reduce antimicrobial resistance and host cell toxicity, ACS Biomater. Sci. Eng. 8 (2022) 1193–1199. https://doi.org/10.1021/acsbiomaterials.1c00876.

[2] H. Gao, T. Tan, D. Wang, Dissolution mechanism and release kinetics of phosphate controlled release glasses in aqueous medium, J. Control. Release. 96 (2004) 29–36. https://doi.org/10.1016/j.jconrel.2003.12.031.

[3] J.S. Fernandes, P. Gentile, R.A. Pires, R. L. Reis, P. V. Hatton, Multifunctional bioactive glass and glass-ceramic biomaterials with antibacterial properties for

repair and regeneration of bone tissue, Acta Biomater. 59 (2017) 2–11. https://doi.org/10.1016/j.actbio.2017.06.046.

[4] M. Vincent, P. Hartemann, M. Engels-Deutsch, Antimicrobial applications of copper, Int. J. Hyg. Environ. Health. 219 (2016) 585–591. https://doi.org/10.1016/j.ijheh.2016.06.003.

[5] S. Akhtach, Z. Tabia, K.E. Mabrouk, M. Bricha, R. Belkhoub, A comprehensive study on copper incorporated bio-glass matrix for its potential antimicrobial applications, Ceram. Int. 47 (2021) 424–433. https://doi.org/10.1016/j.ceramint.2020.08.149

[6] C. M. Ersundu, B. Kuzu, A. E. Ersundu, Structural properties and dissolution behavior of new generation controlled release phosphate glass fertilizers, J. Non Cryst. Solids. 576 (2022) 121239–121243. https://doi.org/10.1016/j.jnoncrysol.2021.121239.

[7] D. Carta, F. Foroutan, J. McGuire, P. Gupta, A. Nikolaou, B. A. Kyffin, N. L. Kelly, J. V. Hanna, J. Gutierrez-Merino, J. C. Knowles, S. Y. Baek, and E. G. Velliou, Antibacterial copper-doped calcium phosphate glasses for bone tissue regeneration, ACS Biomater. Sci. Eng. 5 (2019) 6054–6062. https://doi.org/10.1021/acsbiomaterials.9b01291.

[8] R. Drewello, R. Weissmann. Microbially influenced corrosion of glass, Appl. Microbiol. Biotechnol. 47 (1997) 337–346. https://doi.org/10.1007/s002530050937.

[9] R. Guo, K. Xu, Z. Zhao, C. Niu, H. Li, Effect of the ratio of R =[Na_2O]/[B_2O_3] on the structure, Ag species, and antibacterial activity of Ag-doped borosilicate glass, J. Non Cryst. Solids. 588 (2022) 121610–121615. https://doi.org/10.1016/j.jnoncrysol.2022.121610.

[10] Y. Xu, J. Cheng, W. Zheng, D. Gao, Study on the preparation and properties of silver-doped borosilicate antibacterial glass, J. Non Cryst. Solids. 354 (2008) 1342–1346. https://doi.org/10.1016/j.jnoncrysol.2006.10.085.

[11] A. Nishino, T. Tomioka, M. Arakawa. The Science of Antimicrobial Agents, pt.2, Industrial Research Committee, Tokyo, 1997.

[12] T.M. Gross, J. Lahiri, A. Golas, J. Luo, F. Verrier, J. L. Kurzejewski, D. E. Baker, J. Wang, P. F. Novak, M. J. Snyder, Copper-containing glass ceramic with high antimicrobial efficacy, Nat. Commun. 10 (2019) 1979–1987. https://doi.org/10.1038/s41467-019-09946-9.

[13] K. Schuhladen, X. Wang, L. Hupa, A. R. Boccaccini, Dissolution of borate and borosilicate bioactive glasses and the influence of ion (Zn, Cu) doping in different solutions, J. Non Cryst. Solids. 502 (2018) 22–34. https://doi.org/10.1016/j.jnoncrysol.2018.08.037.

[14] E.A. Neel, I. Ahmed, J. Pratten, S.N. Nazhat, J.C. Knowles, Characterisation of antibacterial copper releasing degradable phosphate glass fibres, Biomaterials. 26 (2005) 2247–2254. https://doi.org/10.1016/j.biomaterials.2004.07.024.

[15] A. Goldstein, M. Vulfson, M. Sirota, Optical spectra of copper-doped Zn-phosphate glasses, J. Am. Ceram. Soc. 90 (2007) 3680–3682. https://doi.org/10.1111/j.1551-2916.2007.01959.x.

[16] J. Gao, R.H. Ma, J.J. Zhao, Q. Xu, X. Qiao, J. Du, X. Fan, Non-bridging oxygen dependent redox and spectroscopic properties of Cu species in phosphosilicate glasses, J. Alloys Compd. 664 (2016) 331–337. https://doi.org/10.1016/j.jallcom.2015.12.041.

[17] A. Chahine, M. Et-tabirou, M. Elbenaissi, M. Haddad, J.L. Pascal, Effect of CuO on the structure and properties of $(50–x/2)Na_2O$-xCuO-$(50–x/2)P_2O_5$ glasses, Mater. Chem. Phys. 84 (2019) 341–347. https://doi.org/10.1016/j.matchemphys.2003.11.009.

[18] J.V. Vondele, M. Krack, F. Mohamed, M. Parrinello, T. Chassaing, J. Hutter, Quickstep: fast and accurate density functional calculations using a mixed Gaussian and plane waves approach, Comput. Phys. Commun. 167 (2005) 103–128. https://doi.org/10.1016/j.cpc.2004.12.014.

[19] T.D. Kuhne, M. lannuzzi, M.D. Ben, V. V. Rybkin, P. Seewald, F. Stein, T. Laino, R. Z. Khaliullin, O. Schütt, F. Schiffmann, D. Golze, J. Wilhelm, S. Chulkov, M. H. Bani-Hashemian, V. Weber, U. Borštnik, M. Taillefumier, A. S. Jakobovits, A. Lazzaro, H. Pabst, T. Müller, R. Schade, M. Guidon, S. Andermatt, N. Holmberg, G. K. Schenter, A. Hehn, A. Bussy, F. Belleflamme, G. Tabacchi, A. Glöß, M. Lass, I. Bethune, C. J. Mundy, C. Plessl, M. Watkins, J. VandeVondele, M. Krack, J. Hutter, CP2K: An electronic structure and molecular dynamics software package-

Quickstep: Efficient and accurate electronic structure calculations, J. Chem. Phys. 152 (2020) 194103–194150. https://doi.org/10.1063/5.0007045.

[20] J.P. Perdew, K. Burke, M. Ernzerhof, Generalized gradient approximation made simple, Phys. Rev. Lett. 77 (1996) 3865–3868. https://doi.org/10.1103/PhysRevLett.77.3865.

[21] S. Grimme, J. Antony, S. Ehrlich, H. Krieg, A consistent and accurate ab initio parametrization of density functional dispersion correction (DFT-D) for the 94 elements H-Pu, J. Chem. Phys. 132 (2010) 154104–154119. https://doi.org/10.1063/1.3382344.

[22] S. Goedecker, M. Teter, J. Hutter, Separable dual-space Gaussian pseudopotentials. Phys. Rev. B. 54 (1996) 1703–1710. https://doi.org/10.1103/PhysRevB.54.1703.

[23] W.G. Hoover, Canonical dynamics: Equilibrium phase-space distributions. Phys. Rev. A. 31 (1985) 1695–1697. https://doi.org/10.1103/PhysRevA.31.1695.

[24] J.A. Jiménez, Luminescent properties of Cu^{+}/Sn^{2+}-activated aluminophosphate glass, Opt. Mater. 37 (2014) 347–351. https://doi.org/10.1016/j.optmat.2014.06.024.

[25] J.A. Jiménez, Spectroscopic inquiry of CuO-doped borate glasses in the $50B_2O_3$-$25Li_2O$-25BaO ternary, Spectrochim. Acta A Mol. Biomol. Spectrosc. 262 (2021) 120113–120123. https://doi.org/10.1016/j.saa.2021.120113.

[26] I. Nakai, C. Numako, H. Hosono, K. Yamasaki, Origin of the red color of satsuma copper-ruby glass as determined by EXAFS and optical absorption spectroscopy,

J. Am. Ceram. Soc. 82 (2004) 689–695. https://doi.org/10.1111/j.1151-2916.1999.tb01818.x.

[27] D. Shiratori, H. Masai, T. Kato, G. Okada, D. Nakauchi, N. Kawaguchi, T. Yanagida, Oxidation suppression of Cu in alkaline aluminophosphate glass and the effects for radiation-induced luminescence characteristics, Sci. Rep. 10 (2020) 21403–21415. https://doi.org/10.1038/s41598-020-78510-z.

[28] L.S. Kau, D.J. Spira-Solomon, J.E. Penner-Hahn, K. O. Hodgson, E. I. Solomon, X-ray absorption edge determination of the oxidation state and coordination number of copper. Application to the type 3 site in Rhus vernicifera laccase and its reaction with oxygen, J. Am. Chem. Soc. 109 (1987) 6433–6442. https://doi.org/10.1021/ja00255a032.

[29] A. Gaur, B.D. Shrivastava, S.K. Joshi, Copper K-edge XANES of Cu(I) and Cu(II) oxide mixtures, J. Phys. Conf. Ser. 190 (2009) 012084–012089. https://doi.org/10.1088/1742-6596/190/1/012084.

[30] F. Farges, M. Etcheverry, A. Scheidegger, D. Grolimund, Speciation and weathering of copper in ‘‘copper red ruby’’ medieval flashed glasses from the Tours cathedral (XIII century), Appl. Geochemistry. 21 (2006) 1715–1731. https://doi.org/10.1016/j.apgeochem.2006.07.008.

[31] M.O. Figueiredo, J.P. Veiga, J.P. MirÃo, Modelling the size of red-colouring copper nanoclusters in archaeological glass beads, Appl. Phys. A 83 (2006) 499–502. https://doi.org/10.1007/s00339-006-3521-4.

[32] J.A. Duffy. Redox equilibria in glass, J. Non Cryst. Solids. 196 (1996) 45–50. https://doi.org/10.1016/0022-3093(95)00560-9.

[33] R. Arletti, M.C. Dalconi, S. Quartieri, M. Triscari, G. Vezzalini, Roman coloured and opaque glass: a chemical and spectroscopic study, Appl. Phys. A 83 (2006) 239–245. https://doi.org/10.1007/s00339-006-3515-2.

[34] H. Takebe, Y. Baba, M. Kuwabara, Dissolution behavior of ZnO–P_2O_5 glasses in water, J. Non Cryst. Solids. 352 (2006) 3088–3094. https://doi.org/10.1016/j.jnoncrysol.2006.04.002.

[35] L. Baia, D. Muresan, M. Baia, J. Popp, S. Simon, Structural properties of silver nanoclusters-phosphate glass composites, Vib. Spectrosc. 43 (2007) 313–318. https://doi.org/10.1016/j.vibspec.2006.03.006.

[36] P. Colomban, A. Tournié, P. Ricciardi, Raman spectroscopy of copper nanoparticle-containing glass matrices: ancient red stained-glass windows, J. Raman Spectrosc. 40 (2009) 1949–1955. https://doi.org/10.1002/jrs.2345.

[37] B. Bae, M.C. Weinberg, Oxidation-reduction equilibrium in copper phosphate glass melted in air, J. Am. Chem. Soc. 74 (1991) 3039–3045. https://doi.org/10.1111/j.1151-2916.1991.tb04299.x.

[38] O. Soriano-Romero, R. Lozada-Morales, A.N. Meza-Rocha, S. Carmona-Tellez, U. Caldino, B. Flores-Desirena, R. Palomino-Merino, Cold bluish white and blue emissions in Cu^{+}-doped zinc phosphate glasses, J. Lumin. 217 (2020) 116791–116798. https://doi.org/10.1016/j.jlumin.2019.116791.

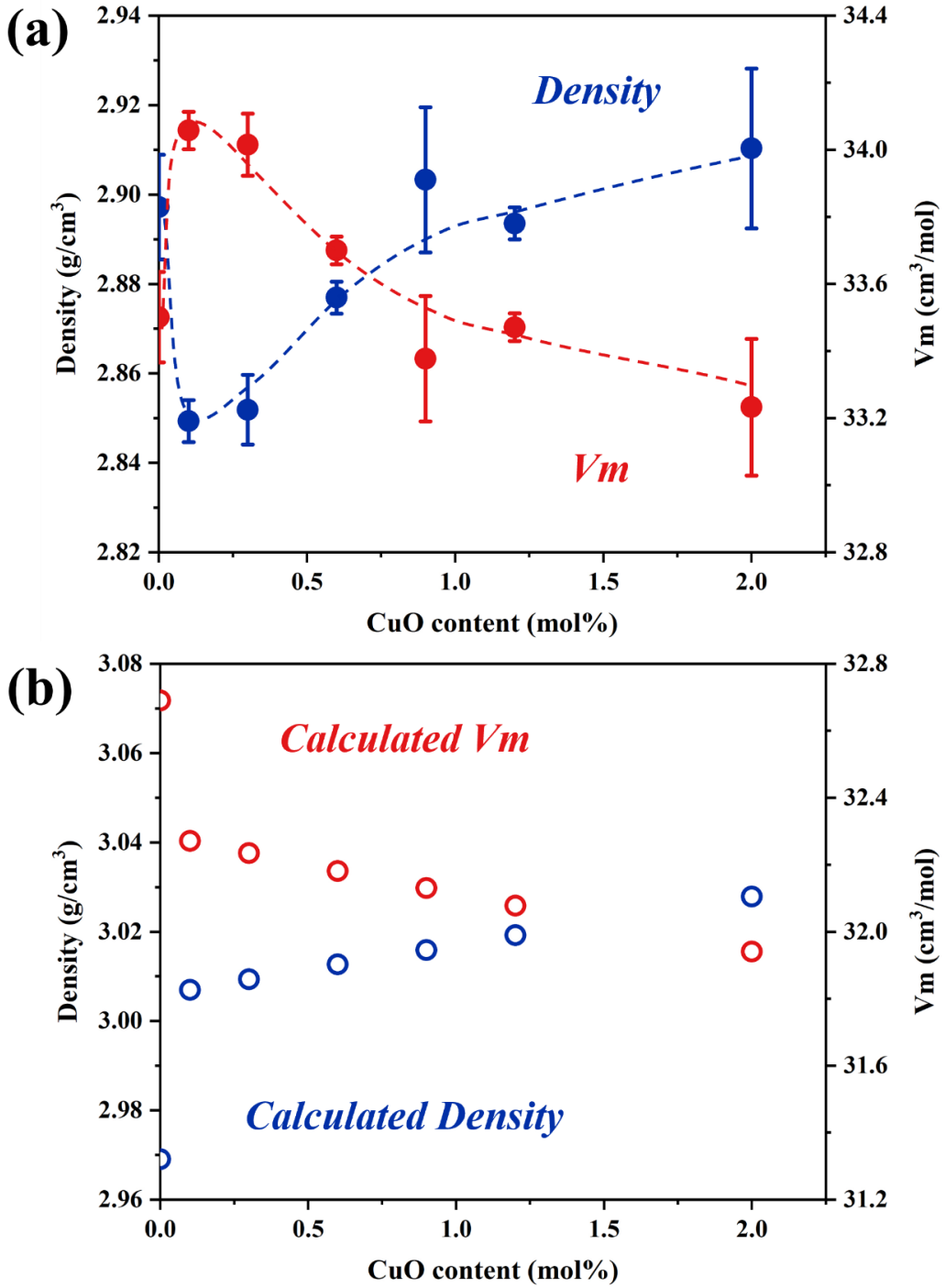

Fig. 1 Density and molar volume (V_m) of glass samples as a function of CuO content. (a) Experimental density and molar volume. The dashed lines represent trend lines. The error bars represent the standard deviation associated with the five repeated measurements. (b) Calculated density and molar volume at 20 °C provided by SciGlass Next Database.

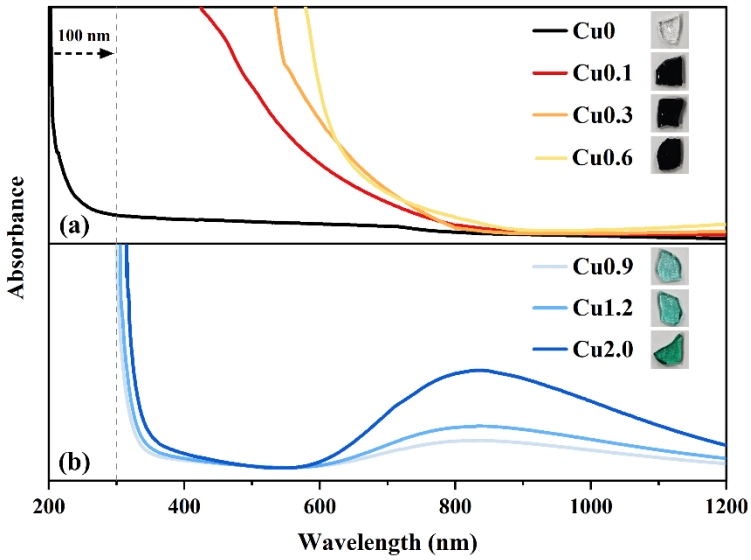

Fig. 2 Optical absorption spectra and images of glasses with CuO contents in the range of (a) 0–0.6 mol% and (b) 0.9–2.0 mol%.

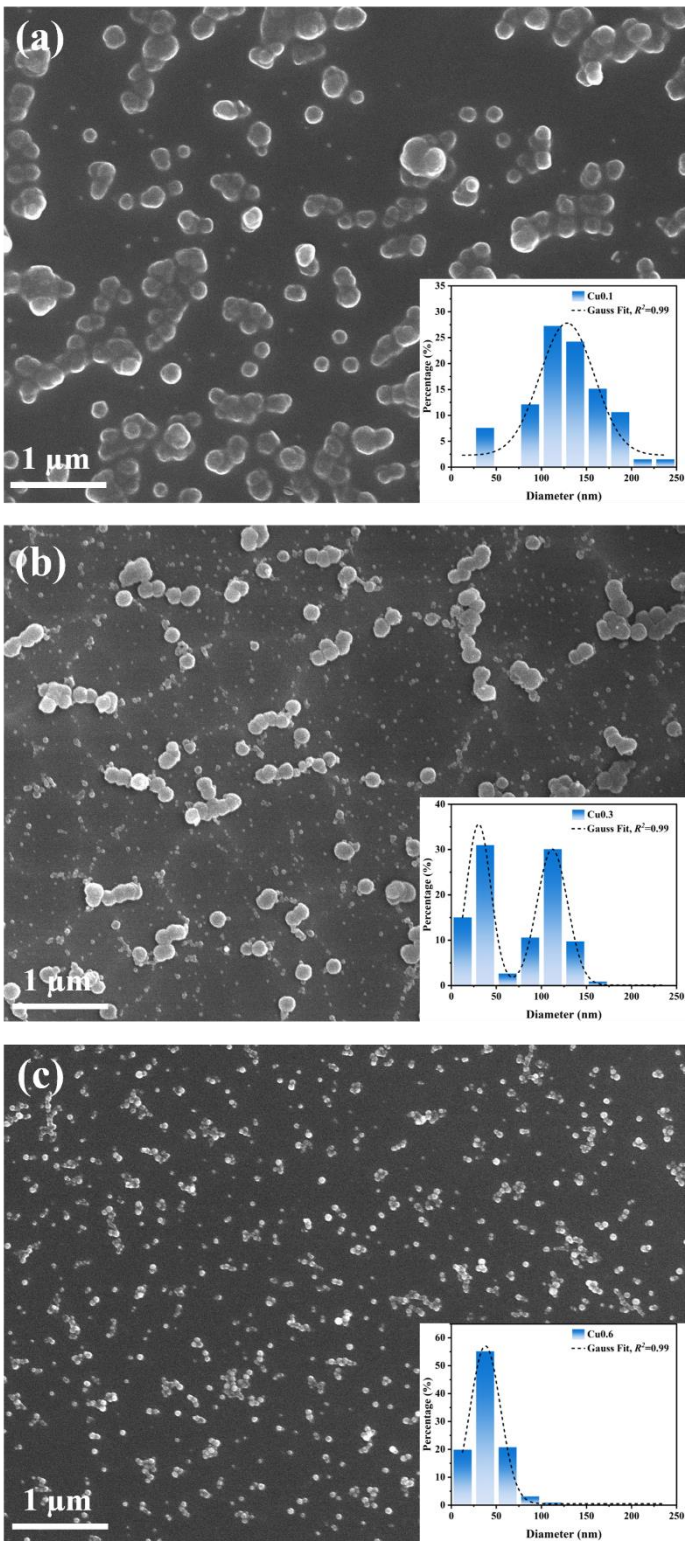

Fig. 3 FE-SEM images of glass samples after 10 min of soaking in HF solution: (a) Cu0.1, (b) Cu0.3, and (c) Cu0.6. The inset figures show the particle size distributions of the particles.

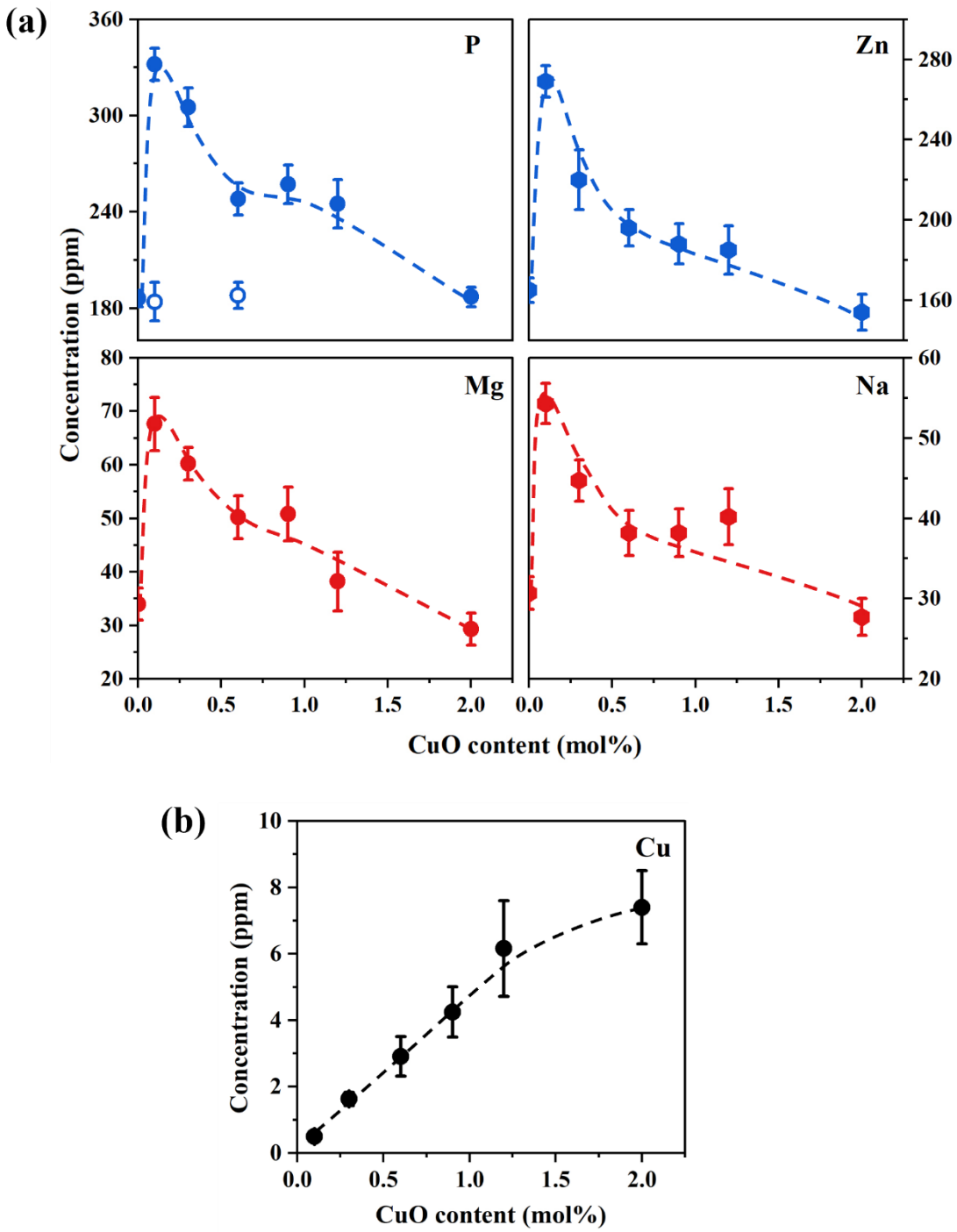

Fig. 4 Elemental concentrations in leachates as a function of CuO content in glasses: (a) P, Zn, Mg, Na and (b) Cu. The dashed lines represent trend lines. The error bars represent the standard deviation associated with duplicate measurements. The hollow dots represent the P release concentrations from the transparent samples Cu0.1 and Cu0.6.

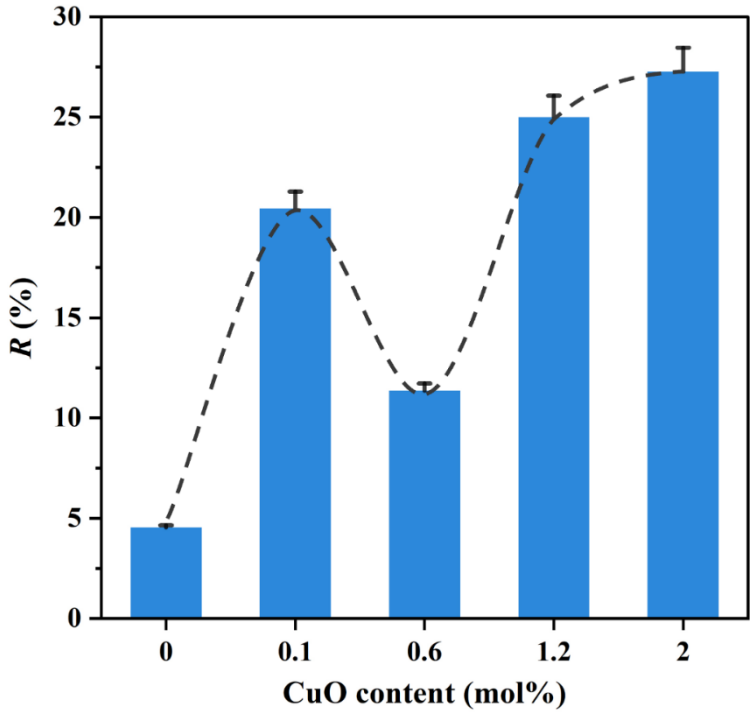

Fig. 5 Bacterial reduction rates (*R*) versus CuO content in glass. The dashed line represents the trend line. The error bars represent the standard deviation associated with triplicate measurements.

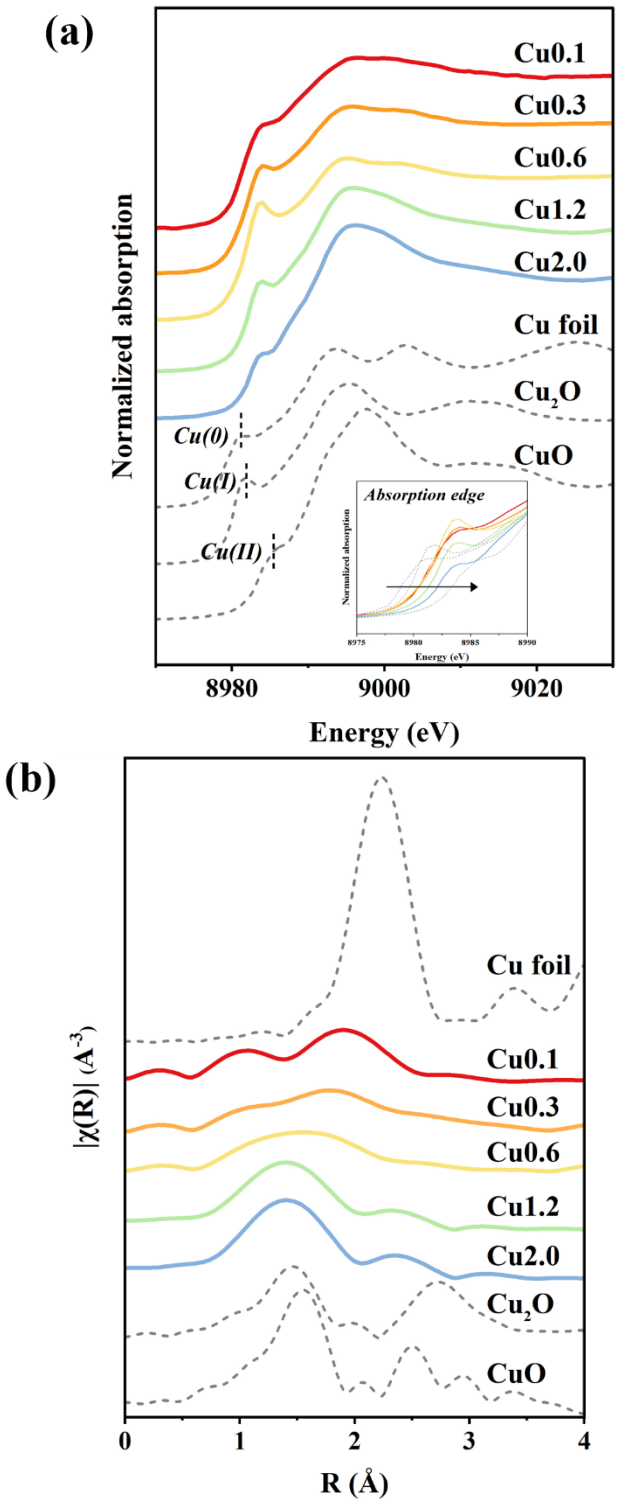

Fig. 6 XAS spectra of Cu-doped glasses with varying CuO contents: (a) Normalized Cu K-edge XANES spectra for Cu-doped glass samples and reference samples Cu foils, Cu_2O, and CuO. The inset figure shows the spectral variation from 8975 to 8990 eV. (b) Fourier transform of the Cu K-edge EXAFS spectra in R space for the Cu-doped glass samples, Cu foils, Cu_2O, and CuO.

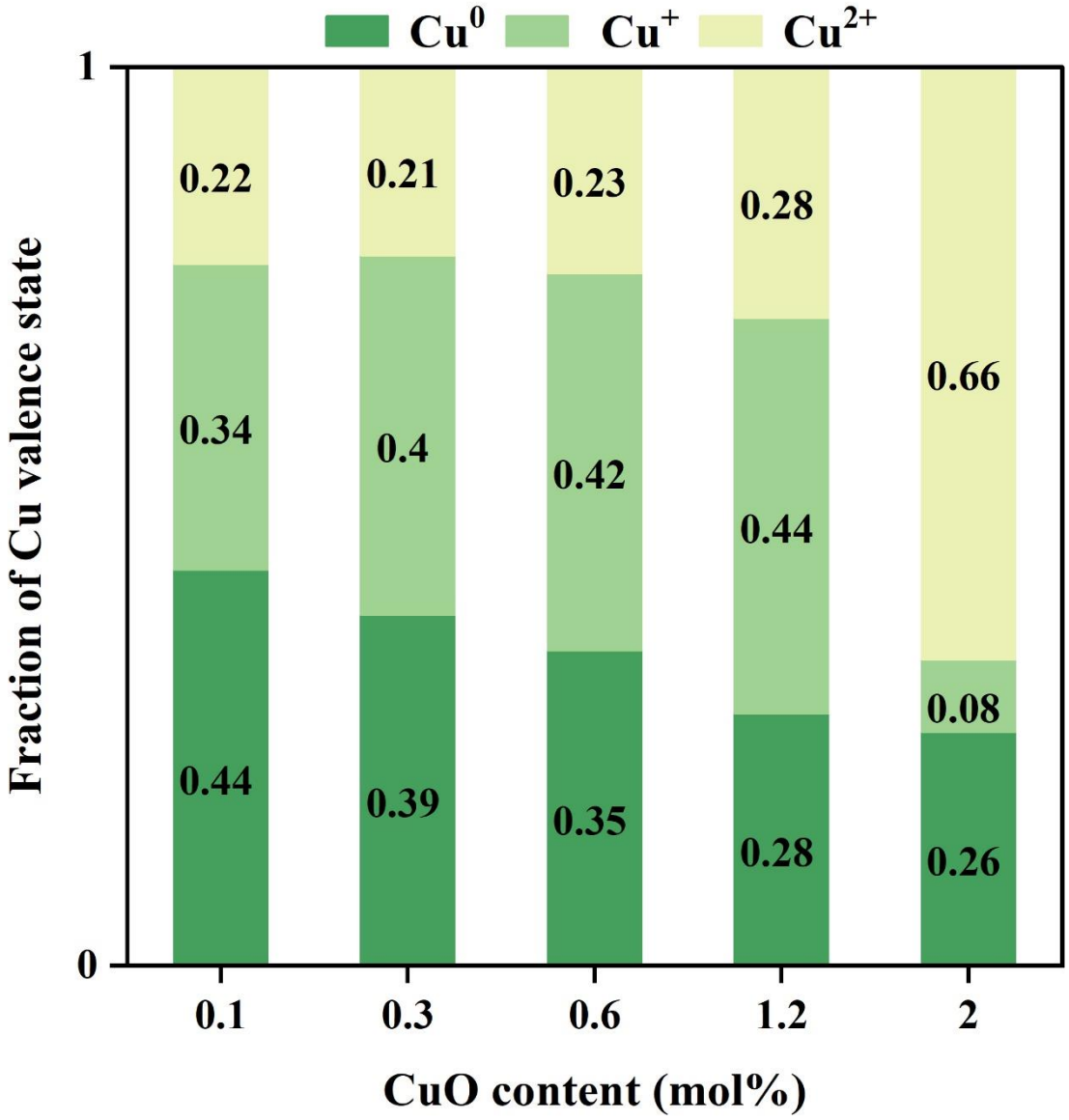

Fig. 7 Fractions of Cu^0, Cu^+, and Cu^{2+} calculated as a function of CuO addition using linear combination fitting of XANES spectra.

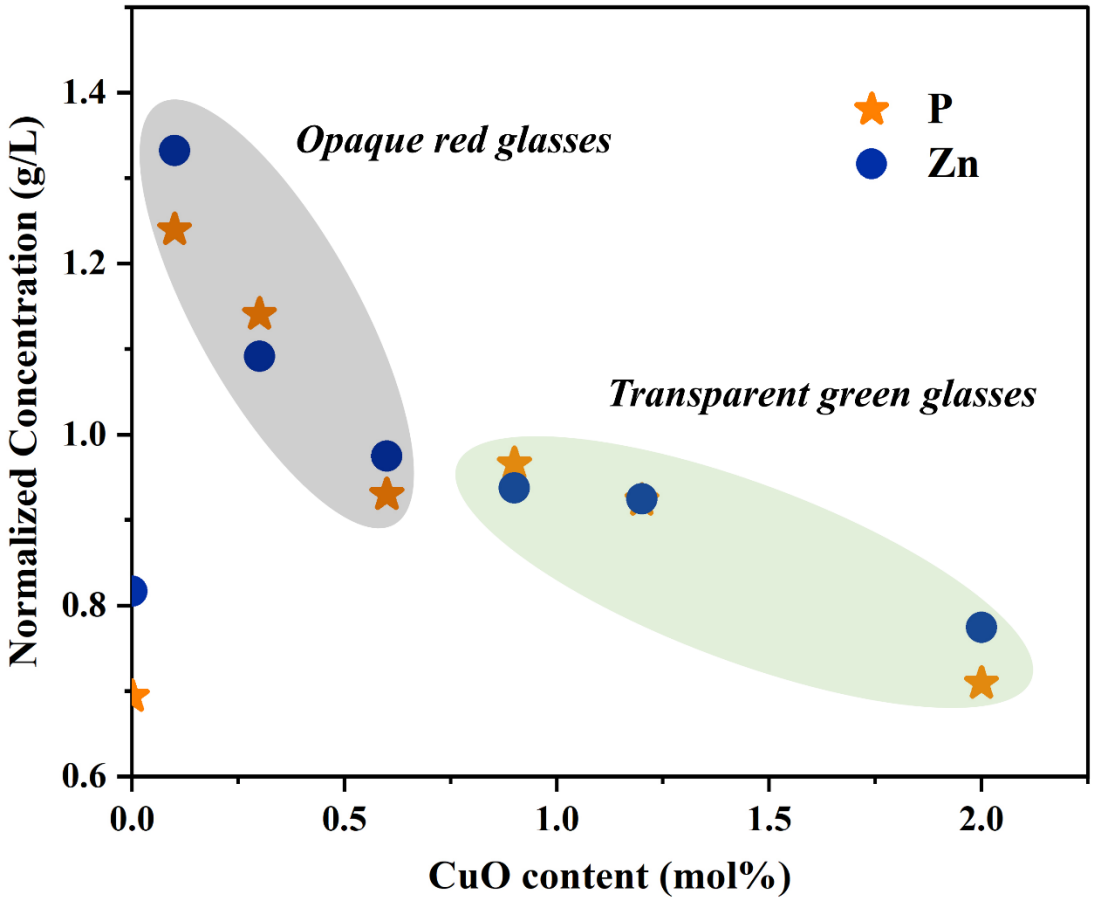

Fig. 8 Normalized concentrations of P and Zn in leachates as a function of CuO content. The error bars are hidden here for better visualization but are consistent with those of the elemental concentrations in the leachates (Fig. 4a).

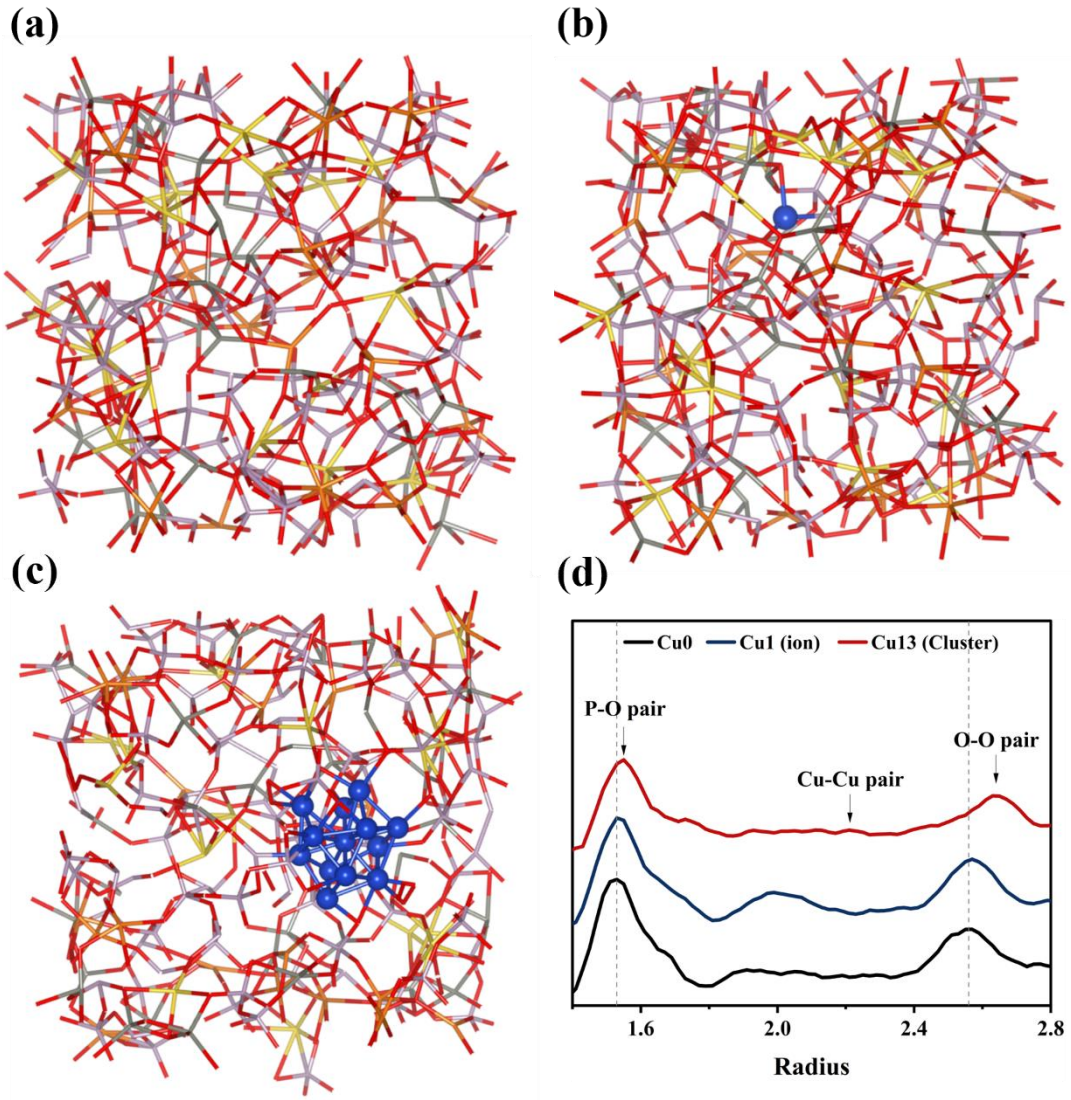

Fig. 9 Structures of three model glass compositions obtained from molecular dynamics simulations: (a) Model base glass Cu0 with composition $42P_2O_5$-30ZnO-20MgO-$8Na_2O$ (mol%). (b) Model glass Cu1 with 1 mol% CuO added. (c) Model glass Cu13 with 13 mol% CuO added, showing Cu atoms forming clusters. (d) Radial distribution functions of glass samples with different Cu species.

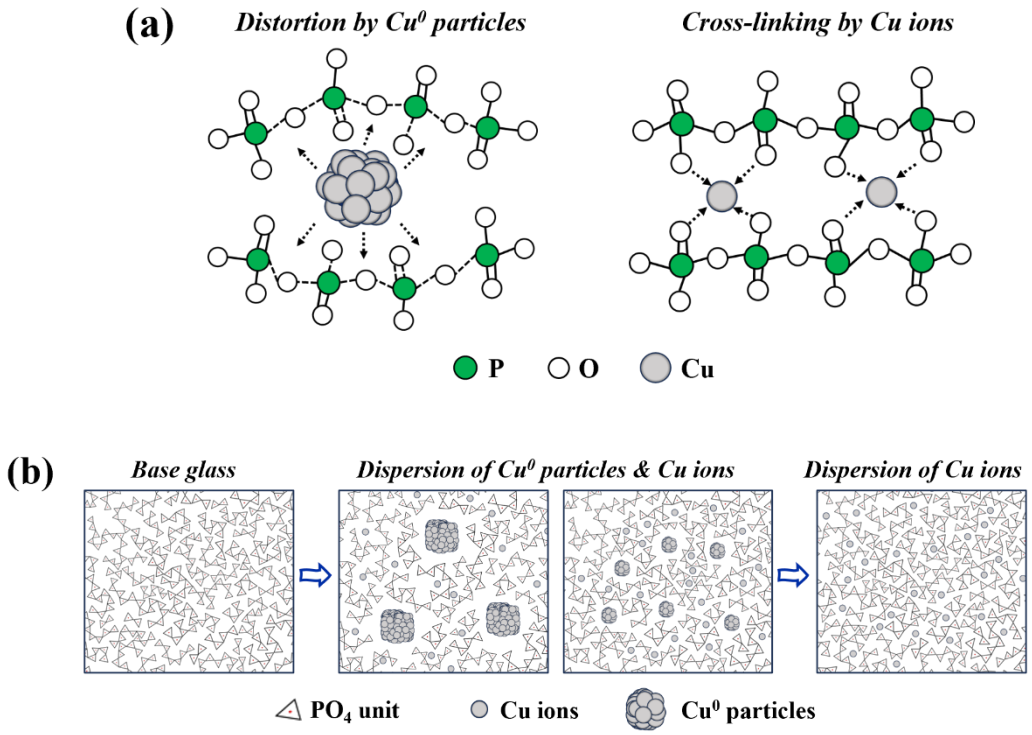

Fig. 10 Schematic representations of the glass structure modified by different Cu species (Cu particles and Cu ions) dispersed in the glass matrix. (a) The impact of different Cu species on the phosphate glass network. (b) Gaps between the glass matrix and different Cu species.